40th AIAA/ASME/SAE/ASEE Joint Propulsion Conference, Fort Lauderdale, Florida, 2004

Self Consistent Electrode Model for Magnetoplasmadynamic Thrusters

Subrata Roy*
Computational Plasma Dynamics Laboratory, Kettering University, Flint, Michigan 48504, USA

Accurate sheath modeling is of considerable interest to the effective design of ionized flow in several aerospace applications including space propulsion thrusters and high-speed air vehicles. In particular, an electrode sheath (fall) voltage model is necessary to predict the power requirement, which in turn is used to measure the total efficiency for on-board propulsion thrusters. Plasma wall interaction is thus crucial for improving the high power thruster efficiency. In this paper, a finite element discretized two-dimensional self-consistent formulation of plasma–sheath dynamics, using multi-fluid equations for partially ionized plasma, is presented. The formulation is applied to a simplistic electrode model. Computed potential distributions on three locations along the electrode are plotted. The details of the number densities of electrons, ions and neutrals along with ion, electron and neutral dynamics, sheath potential and electron temperature profiles gives insight into the wall potential loss mechanism.

Nomenclature

A	=	coefficient
$\mathbf{B}$, B	=	magnetic field
E_i	=	first ionization potential
$\mathbf{E}$, E	=	electric field
e	=	elementary charge
$\mathbf{J}$, J	=	current
k_B	=	Boltzmann constant
m	=	electron mass
M	=	ion mass
m_n	=	neutral mass
n	=	species number density
n^i	=	degree of ionization
p	=	pressure
S	=	ionization, recombination
T	=	temperature (eV)
t	=	time
$\mathbf{V}$, V	=	velocity
V_B	=	Bohm velocity
w	=	test functions
Z	=	ionicity
α	=	coefficient
χ	=	Planck's constant
ε	=	specific energy

* Associate Professor of Mechanical Engineering, 1700 West Third Avenue, and AIAA Associate Fellow.

γ = specific heat ratio
λ = bulk viscosity
η = molecular viscosity
μ_0 = permittivity
ν = collision frequency
Ω = computational domain
Ω_e = computational element
σ = domain envelop, conductivity

Subscripts
e = electron
i = ion
ioniz = ionization
n = neutral
R = radiation
r = radial direction
recomb = recombination
w = wall losses
z = axial direction
α = e,i
θ = azimuthal direction

I. Introduction

SHEATH modeling is pivotal for designing of ionized flow in several magnetoplasmadynamic (MPD) applications including space propulsion thrusters and high-speed air vehicles. Present status of the space propulsion and hypersonic flow research reflects a need of consistent numerical models to understand the wall loss mechanism for bounded plasma in the presence and absence of a magnetic field. The anomalies are primarily due to the choice of sheath edge (Bohm criterion) as the boundary condition for both plasma and sheath using an inconsistent model. There are several theoretical sheath models available in the literature. However, none of these models include the ionization and recombination process in the presence of neutrals that is of practical significance. Our application interest is MPD thrusters. These are of considerable interest to the NASA Earth Science, Space Science, and Human Exploration and Development of Space Strategic Enterprises for developing high-power in-space electric propulsion systems. In this device, the gaseous propellant is ionized by an arc current that interacts with the self-induced or applied magnetic field to accelerate the plasma, and produces the required thrust through an inherently unsteady process. The present work has originated from the need of a physics-based wall model in a multiblock arbitrary coordinate hydromagnetic (MACH) family of complex geometry codes[1] for predicting electrode fall voltages, material erosion and sublimation, and the onset of thruster instabilities. The MACH codes are developed by the Center for Plasma Theory and Computation at the Air Force Research Laboratory[2] and have been utilized for the performance evaluation of self-field and applied-field MPD thrusters over a wide range of operating parameters.[3-5] Besides MACH codes there are other reported numerical developments that use physics based transport models crucial for designing applied and self-field operations for simulating practical thruster geometries and ionized real gas at high power (~0.1MW-1MW).

These efforts range from utilizing finite difference methodology to solve the fully ionized MPD equations with ideal gas equation of state[9] to the finite volume methodology for solving the velocity, pressure, electron-ion temperature and current field equations.[8,10] Documented results in most of these papers were compared with experimental thrust data. The difference between characteristic time scale of fluid-thermal (msec) and electromagnetic (μsec) effects are also considered by computational models.[11] A detail comparison of thrust versus current curves for various mass flow rates is presented in Ref. 12. These results show a wide variation of numerical solution accuracy for DT series and hot anode thrusters (HAT). A combined Galerkin and least squares (GLS) finite element approach has also been presented for a two-dimensional steady state operation.[13] The Galerkin method was used to analyze the single fluid Navier-Stokes regime subjected to electromagnetic forces, while the least squares solved the Maxwell's equations. The applied field MPD thruster was simulated with two-dimensional electromagnetic equations with quasi-one-dimensional fluid equations to examine applied-field acceleration mechanism.[14] The analysis showed that substantial Hall currents and plasma rotation were produced from interaction

of the applied field with discharge current. However, most MPD thruster simulations[5-14] lack an self-consistent electrode sheath (fall) voltage model necessary to predict the total thruster voltage, which in turn is required to predict total thruster efficiency. In this paper, a finite element discretized two-dimensional self-consistent formulation of plasma–sheath dynamics, using multi-fluid equations for a partially ionized plasma inside the thruster, is presented.

The theoretical basis of this work has been initiated by studying the one dimensional plasma-sheath including space charge effects in Ref. 15-16. The model incorporated space charge effect throughout the whole plasma and the sheath region using multi-fluid equations. Secondary electron emission and induced magnetic field effect was not considered. The applications included dc and rf sheath inside a glow discharge tube where the noble gas is immobile, and a partially ionized plasma sheath inside an electric propulsion thruster channel in which the gas flows. Representative solutions of the electron and ion number densities[16] show the expected quasi neutrality in the bulk and charge separated region near the anode (left) and the cathode (right), Fig. 1a. The computed sheath potential in Fig. 1b shows excellent comparison with the available experimental data.[17] Under the influence of this potential, ions accelerate toward the negatively charged wall and reach the characteristic velocity V_{GS} given by Godyak and Sternberg[18] at the presheath-sheath boundary. The ion velocity keeps increasing inside the sheath exceeding Bohm velocity and it finally saturates at the wall. The reduction of ion density inside the sheath can be correlated with the increase in the ion velocity. As a continuation to our previous efforts, specific study for two-dimensional MPD thruster channel with the inclusion of anode and cathode sheath model is attempted here. The results should be qualitatively comparable with the reported experimental data and simulation results in high power thrusters.

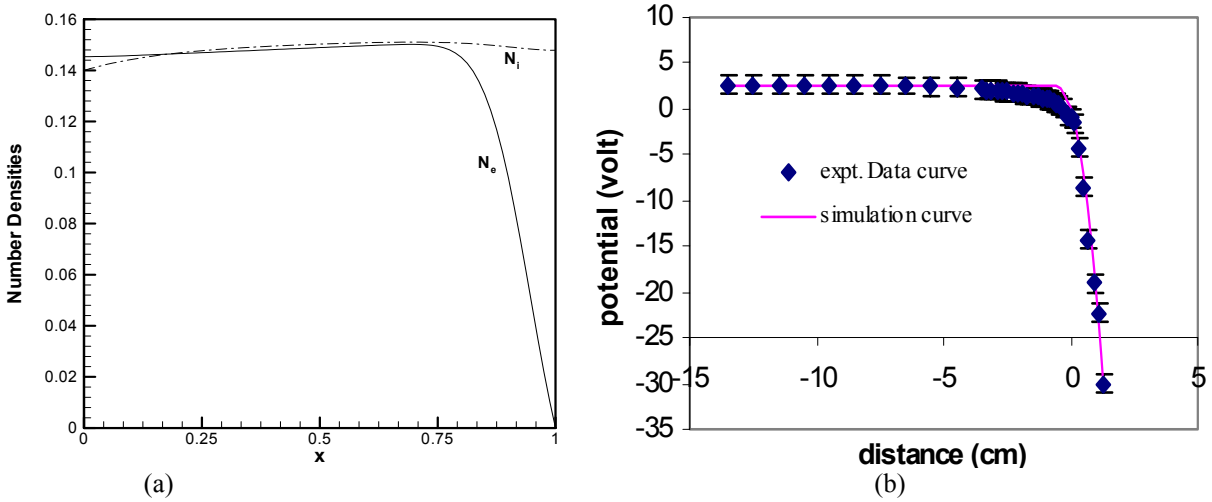

(a) (b)

Figure 1. Plasma sheath solution from Ref. 16. (a) Electron and ion number densities, (b) Potential distribution is compared with experimental data.[17]

II. Magnetohydrodynamics

The following two-dimensional, compressible form of three fluids plasma equation is an extension of our earlier work[16,19] and is solved without considering the secondaries and sputter yield. The magnetic field is only considered in the azimuthal direction.

A. The Continuity Equations

$$\frac{\partial n_e}{\partial t}+\frac{\partial}{\partial r}(n_eV_{er})+\frac{\partial(n_eV_{ez})}{\partial z}=S_{ioniz}-S_{recomb}-\frac{n_eV_{er}}{r}$$

$$\frac{\partial n_i}{\partial t}+\frac{\partial}{\partial r}(n_iV_{ir})+\frac{\partial(n_iV_{iz})}{\partial z}=S_{ioniz}-S_{recomb}-\frac{n_iV_{ir}}{r}$$

$$\frac{\partial n_n}{\partial t}+\frac{\partial}{\partial r}(n_nV_n)+\frac{\partial(n_nV_{nz})}{\partial z}=-S_{ioniz}+S_{recomb}-\frac{n_nV_{nr}}{r}$$

$$S_{ioniz} = RSn_e n_n;\ \ S_{recomb} = Rn_e^2 n_i; R = 8.25\times10^{-43} e^{1.6276}\left(\log\frac{T_e}{1000} - 3.95\right)^2; S = 2.9\times10^{22} T_e^{1.5} \exp\left(\frac{-eE_i}{T_e}\right)$$

B. The Momentum Equations

Due to inertia the electrons are considered at steady state with respect to the ions and neutrals, and obey the following momentum equations.

$$E_r = V_{iz} B_\theta - \frac{1}{\sigma\mu_0}\frac{\partial B_\theta}{\partial z} + \frac{1}{en_e}\left(\frac{\partial p_e}{\partial r} - \frac{1}{\mu_0}\left(\frac{1}{2}\frac{\partial B_\theta^2}{\partial r} + \frac{B_\theta^2}{r}\right)\right),$$

$$E_z = -V_{ir} B_\theta + \frac{1}{\sigma\mu_0}\left(\frac{\partial B_\theta}{\partial r} + \frac{B_\theta}{r}\right) + \frac{1}{en_e}\frac{\partial}{\partial z}\left(p_e - \frac{B_\theta^2}{2\mu_0}\right)$$

The ion momentum equation is time dependent.

$$\frac{\partial \rho\mathbf{V}}{\partial t} + \nabla\cdot(\rho\mathbf{V}\mathbf{V}) = -\nabla p + J\times B + \eta\left[\nabla^2\mathbf{V} + \nabla(\nabla\bullet\mathbf{V})\right] + 2(\nabla\eta\bullet\nabla)\mathbf{V} + \nabla\eta\times(\nabla\times\mathbf{V}) - \frac{2}{3}\nabla\left[\eta(\nabla\bullet\mathbf{V})\right]$$

The above equation can become cumbersome when expanded in the component form. For example, the radial component of the ion momentum equation may be written as

$$n_i M\left(\frac{\partial V_{ir}}{\partial t} + V_{ir}\frac{\partial V_{ir}}{\partial r} + V_{iz}\frac{\partial V_{ir}}{\partial z} - \frac{V_{i\theta}^2}{r}\right) = -\frac{\partial p_i}{\partial r} - f\left(\frac{\partial p_e}{\partial r} - \frac{1}{\mu_0}\left(\frac{1}{2}\frac{\partial B_\theta^2}{\partial r} + \frac{B_\theta^2}{r}\right)\right) - V_{ir}\left(\frac{4}{3}\frac{\eta}{r^2} + \frac{2}{3r}\frac{\partial\eta}{\partial r}\right) + \frac{4}{3}\frac{\partial V_{ir}}{\partial r}\left(\frac{\eta}{r} + \frac{\partial\eta}{\partial r}\right) + \frac{\partial V_{ir}}{\partial z}\frac{\partial\eta}{\partial z} + \frac{4\eta}{3}\frac{\partial^2 V_{ir}}{\partial r^2}$$

$$+\eta\frac{\partial^2 V_{iz}}{\partial z^2} + \frac{\eta}{3}\frac{\partial^2 V_{iz}}{\partial r\partial z} + \frac{\partial\eta}{\partial z}\frac{\partial V_{iz}}{\partial r} - \frac{2}{3}\frac{\partial\eta}{\partial r}\left(\frac{\partial V_{iz}}{\partial z}\right) + mn_i\nu_{ei}(V_{er} - fV_{ir}) - \frac{m_n}{M+m_n} n_i M\nu_{in}(V_{ir} - V_{nr}) + \left(S_{recomb} - S_{ioniz}\right)MV_{ir} + Mn_i\nu_{\mathbf{w}}V_{ir},$$

where $f=n_i/n_e$. Note that the electron-ion and ion-neutral collisional momentum transfers are included in the above form. The details of these equations will be given later in a more elaborate paper.

Here, the viscosity is given as

$$\eta = 1.25\times10^{-19}\frac{5}{8n^i A}\left(\frac{mMT_i}{\pi}\right)^{0.5}\left(\frac{2T_i}{e^2}\right)^2$$

For a singly ionized plasma $n^i = 1$ and

$$A = 2\left[\ln(1+\alpha^2) - \frac{\alpha^2}{1+\alpha^2}\right] = 0.385$$

, for $\alpha = 1$. The neutral velocity V_n is assumed constant.

C. The Energy Equations

For the specific energy ε_α of species α

$$\varepsilon_\alpha = \frac{p_\alpha}{\gamma-1} + \frac{\rho V^2}{2} + \frac{B^2}{2\mu_0}$$

, the following electron and ion energy equations are used.

Ion energy:

$$\rho\left[\partial_t + V\bullet\nabla\right]\varepsilon_i\cdot = -p\nabla\cdot V + \nabla\cdot(\kappa_i\nabla T_i) + \rho\nu_{ei}C_V(T_e - T_i) + S(\eta,\lambda) + \Delta Q_{ei}$$

Here, $$S(\eta,\lambda) = \eta\left(2\left[\left(\frac{\partial V_{ir}}{\partial r}\right)^2 + \left(\frac{V_{ir}}{r}\right)^2 + \left(\frac{\partial V_{iz}}{\partial z}\right)^2\right] + \left(\frac{\partial V_{i\theta}}{\partial z}\right)^2 + \left(\frac{\partial V_{ir}}{\partial z} + \frac{\partial V_{iz}}{\partial r}\right)^2 + \left(\frac{\partial V_{i\theta}}{\partial r} - \frac{V_{i\theta}}{r}\right)^2\right) + \lambda\left(\nabla\bullet\mathbf{V}\right)^2$$ with Stokes hypothesis $\eta + 1.5\lambda = 0$ and the collisional energy transfer is given as $\Delta Q_{ei} = 3\frac{m}{M}\rho_i R\left(T_e - T_i\right)\nu_{ei}$.

Electron energy:

$$\rho\left[\partial_t + V\bullet\nabla\right]\varepsilon_e\cdot = -p_e\nabla\cdot V + \eta J^2 - \mathbf{J}\bullet\left(\frac{\nabla p_e}{en_e}\right) + \nabla\cdot(\kappa_e\nabla T_e) - \rho\nu_{ei}C_V(T_e - T_i) - ac\rho\chi_{planck}(T_e^4 - T_R^4)$$

which in expanded form can be written as

$$1.5\, n_e \left[\frac{\partial}{\partial t}+V_{er}\frac{\partial}{\partial r}+V_{er}\frac{\partial}{\partial r}\right]T_e + T_e\left(\frac{\partial V_{er}}{\partial r}+\frac{V_{er}}{r}+\frac{\partial V_{ez}}{\partial z}\right)++\frac{\sigma}{\mu_0}\left(\frac{\partial B_\theta}{\partial r}+\frac{B_\theta}{r}-\frac{\partial B_\theta}{\partial z}\right)^2+\left(\frac{1}{e\mu_0}\right)\left(\frac{\partial B_\theta}{\partial z}-\left(\frac{\partial B_\theta}{\partial r}+\frac{B_\theta}{r}\right)\right)$$

$$\left(\frac{\partial T_e}{\partial r}+\frac{1}{n_e}\frac{\partial n_e}{\partial r}\right)+\left(\frac{\partial \kappa_e}{\partial r}+\frac{\kappa_e}{r}\right)\frac{\partial T_e}{\partial r}+\kappa_e\frac{\partial^2 T_e}{\partial r^2}-n_i M\nu_{ei}C_V(T_e-T_i)-ac\rho\chi_{planck}(T_e^4-T_R^4)-\left(S_{ioniz}-S_{recomb}\right)\left(E_i-1.5T_e\right)$$

Above, the conductivities and collision frequencies are given as

$$\kappa_e \approx 2.55\times10^{-10}\frac{T_e^{2.5}}{\ln\Lambda_e};\ \kappa_i \approx 1.35\times10^{-12}\frac{T_i^{2.5}}{\ln\Lambda_i};\ \nu_{ei}=1.836\times10^{-6}\frac{\rho\ln\Lambda_e}{MT_e^{1.5}};\sigma=10^3\frac{\ln\Lambda_e}{1.53T_e^{1.5}}$$

Here, the Coulomb logarithm is
$$\ln\Lambda_e \approx 23-\ln\left(\frac{1.22\times10^3 n^{1/2}}{T_e^{3/2}}\right)$$

The neutrals are considered cold. The radiation energy equation is not solved and a reference T_R is assumed.

D. The Electromagnetic Equations

The induction equation is
$$\partial_t\mathbf{B}=\nabla\times(\mathbf{V}\times\mathbf{B})-\nabla\times(\sigma\mathbf{J})-\nabla\times\left(\frac{\mathbf{J}\times\mathbf{B}}{en_e}\right)+\nabla\times\left(\frac{\nabla p_e}{en_e}\right)$$

with the current density components as

$$J_r=-\frac{1}{\mu_0}\frac{\partial B_\theta}{\partial z},\ J_z=\frac{1}{\mu_0}\frac{\partial B_\theta}{\partial r}+\frac{B_\theta}{\mu_0 r}$$ which means $$V_{er}=fV_{ir}-\frac{J_r}{n_e},\ V_{ez}=fV_{iz}-\frac{J_z}{n_e}$$

The criterion $\nabla\bullet\mathbf{B}=\mathbf{0}$ is also verified. The following potential equation is used,

$$\nabla^2\phi=\nabla.(\mathbf{V}\times\mathbf{B})-\eta\nabla\bullet\mathbf{J}-\nabla\bullet\left(\frac{\mathbf{J}\times\mathbf{B}}{en_e}\right)-\nabla\bullet\left(\frac{\nabla p_e}{en_e}\right)$$

For the charge separated region of ionicity $Z = 1$, the potential equation without the influence of B_θ may be written as

$$\frac{\partial^2\phi}{\partial r^2}+\frac{1}{r}\frac{\partial\phi}{\partial r}+\frac{\partial^2\phi}{\partial r^2}=\frac{e(Zn_i-n_e)}{\varepsilon_0}$$. The electric field is derived as

$$\mathbf{E}=-\nabla\phi-\frac{\partial\mathbf{A}}{\partial t}$$

Here, Coulomb gauge condition is $\nabla.\mathbf{A}=\mathbf{0}$. Finally, the equation of state is given as

$$p_{e,i}=n_{e,i}T_{e,i}$$

E. Thrust Calculation

A modified Maecker formula[20] is used to calculate the total thrust.

$$T=\frac{(\gamma+1)\mu_0 J^2}{8\pi}+\frac{8\pi V_B^2\dot{m}^2}{\gamma^2\mu_0 J^2}$$

Besides axial Lorentz force (**j** × **B**), the above equation includes the body force generated by the Ohmic heating.

III. Numerical Method

A finite element based numerical code is used to solve the plasma-sheath problem inside the thruster. The code is modular and has been used to solve a range of problems involving collisional plasmas[15,16,19,21,22] and micro/nanoscale flows.[23-25] Briefly, the variational integral using any admissible test function *w* yields the *weak statement* for the governing continuity, momentum and energy equations. Thereafter, the domain Ω and integrated variables are spatially discretised to Ω_e and solution variables are locally interpolated using Lagrange basis functions.

The weak statement naturally yields the surface integrals via application of Green-Gauss theorem, which contains the unknown boundary fluxes wherever Dirichlet (fixed) boundary conditions are enforced. The zero gradient boundary conditions are automatically enforced via removal of the surface integral. For non-homogeneous wall fluxes, appropriate surface integrals are replaced by incorporating the current conditions into the momentum and energy equations. The terminal ODE is usually solved using a Newton-Raphson scheme and iterated at each until a specified convergence criteria of relative solution norm $<10^{-4}$ is met.

The difficulty involved in achieving a steady state solution of equation described in Section II directly is due to the stiffness of the final matrix and the selection of initial conditions. The computational geometry for this study is discretised using 840 two-dimensional 9-noded biquadratic finite elements consisting of 3485 nodes. The calculations are done based on staggered mesh approach.

IV. Results and Discussion

The computed results for the thruster are presented in this section. The schematic of the axisymmetric computational domain is shown in Fig. 2. The inlet boundary is located at the left end and the electrode locations are shown. The cathode radius is 1cm and the inter-electrode spacing is 6cm. The lengths of cathode and anode are 9cm and 11cm, respectively. The total domain length is 15cm. Symmetry boundary conditions are applied at the bottom surface beyond the cathode tip where the radial and the inductive components are zero. The outflow condition is at the right end and at the top surface beyond the anode wall. Homogeneous gradient (adiabatic) wall boundary condition is applied to the electrodes. Argon gas at 5.8 g/s at 0.4 eV is injected at the inlet. For the current of 16 kA, the solutions are plotted in Figures 3-6.

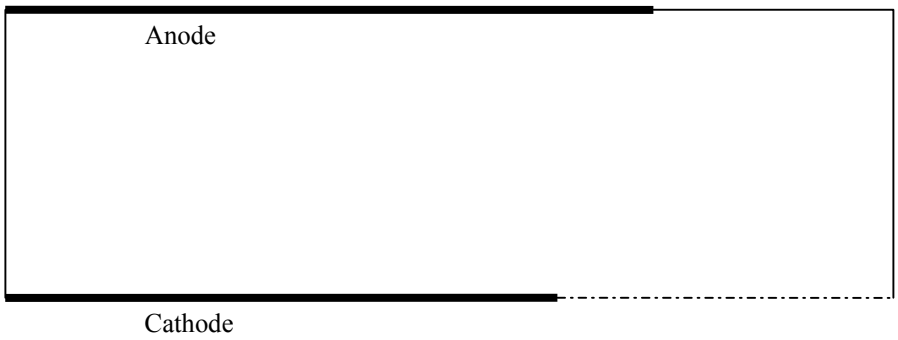

Figure 2. Schematic of the solution domain.

Figure 3 describes the electron temperature, the neutral gas density and the electron density along the channel. The temperature in Fig. 3a varies from 0.4eV at the inlet to approximately 5ev just downstream of the cathode tip. The results are similar to that reported by other experiments and simulations. The neutral number density in Fig. 3b decays sharply beyond the inlet and nearly 90% near the electrodes. While this compares favorably with reported ionization results,[3,6,8,12] the profile does not seem to directly correlate with neither the temperature nor the electron number densities plotted in Fig. 3a and 3c, respectively. Note the "cathode jet" shown in red color near the cathode with electron number densities close to 10^{22} m^{-3}, while near the anode fewer electrons (4×10^{19} m^{-3}) are noticeable. This contours compares well with photographically recorded argon ion emission using an FSBT with transparent walls as reported in the literature.[26]

Figure 4 plots the axial velocity and current contours. The axial velocity ranges from 1 km/s near the inlet to about 20 km/s downstream of the cathode tip. The very high velocity at the line of symmetry indicates a pinching effect due to the radial component of the electromotive force $\mathbf{J}\times\mathbf{B}$. Figure 4b displays severe current distention downstream of the discharge chamber with values in the excess of 1000 Amps/cm^2 extending well into the plume region. This implies a low magnetic Reynolds number flow with a diffuse arc and thus a significant electrothermal contribution. Indeed, a comparison between the electromagnetic and electrothermal contribution to the axial kinetic power confirms an approximately equal contribution. This is a consequence of the electron-atom contribution to the electrical diffusivity of the plasma that in effect decreases the effective magnetic Reynolds number by two orders of magnitude.

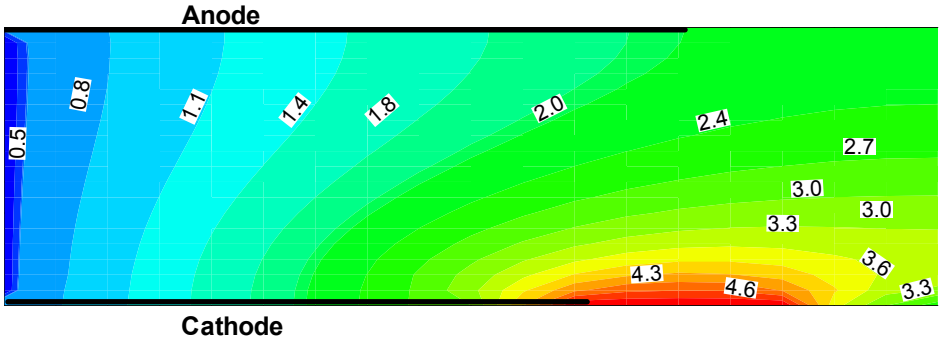

(a) Electron temperatures in eV

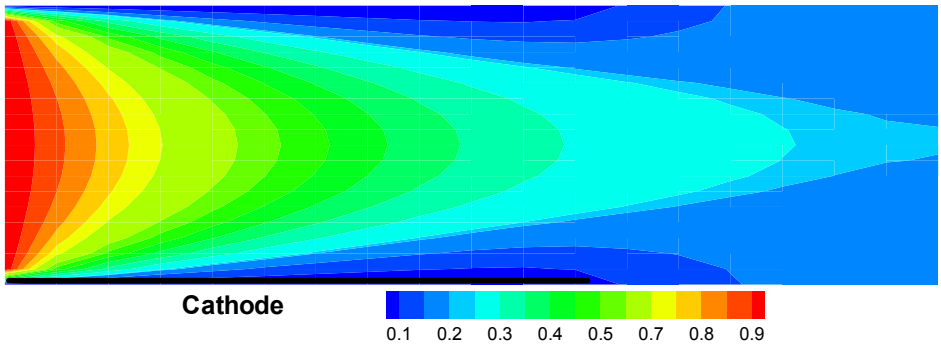

(b) Neutral gas density normalized by inlet density

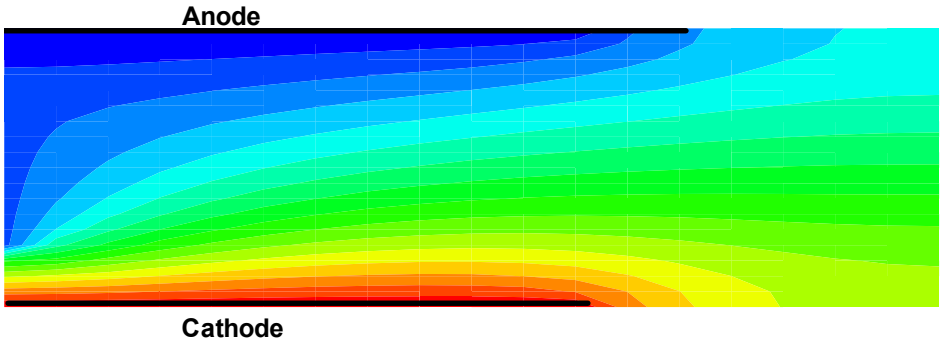

(c) Electron number density distribution

Figure 3. Electron temperature, neutral gas density and electron number density distribution inside the thruster channel.

The potential contours plotted in Figure 5 shows the sheath formation near the electrodes. To the best of this author's knowledge, this was not captured before. The results plot a sharp drop of potential near the cathode and smaller drop at the anode. The fall voltage increases along the length of the electrode and is nearly 50% of the total voltage drop across the flow. Figure 6a plots the crosswise distribution of potential at three locations along the channel. At the downstream location near the thruster exit a fluctuation in the potential is predicted which may in turn give rise to an electrical double layer. The temperature distributions along the same locations are also presented in Fig. 6b and show the rapid rise in energy at the centerline just upstream of the channel exit. Finally, based on modified Maecker's formula the thrust is calculated to be 49.2 N. Note that this number is close to the Princeton experimental data.[27] However, their mass flowrate is 6 g/s, which is slightly higher. Also their anode geometry is quite different and the thruster includes a dielectric wall.

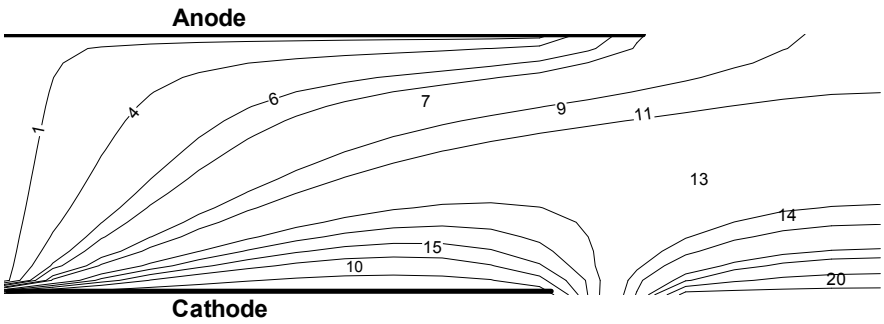

(a) Axial velocity in km/s

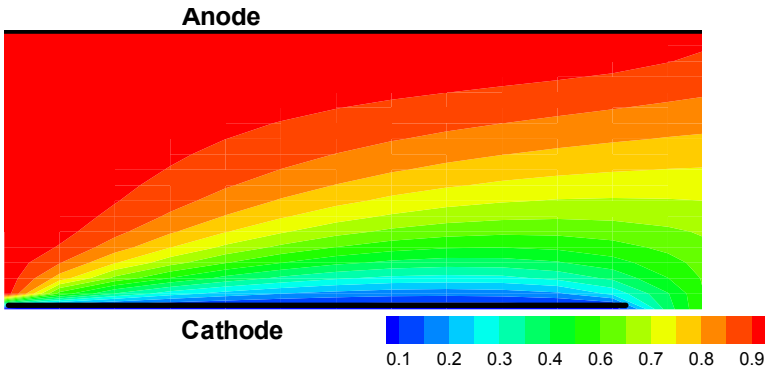

(b) Current distribution inside the channel normalized by the inlet

Figure 4. Velocity and current distributions inside the thruster and downstream.

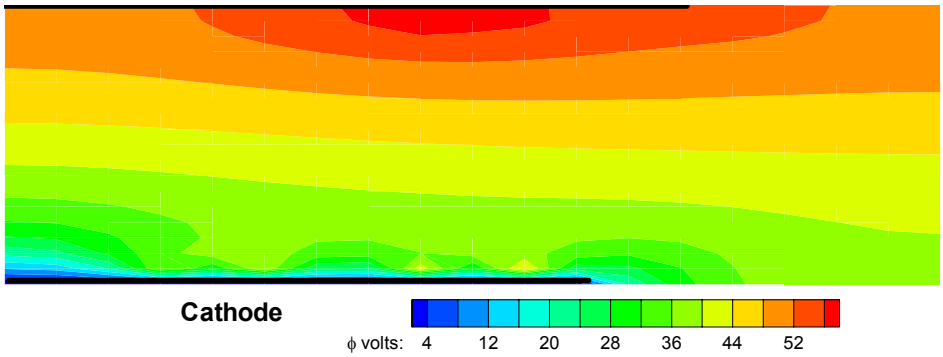

Figure 5. Contours of potential along the thruster show presence of sheath and fall voltage.

V. Conclusions

A two dimensional, compressible form of three fluids, two momentum and two energy plasma sheath model is developed using finite element technique and applied for low pressure space plasma inside an MPD thruster. The model is solved without considering the secondaries and sputter yield. The results qualitatively compare well with the other reported experimental and simulation data. The model needs to be validated thoroughly with available experimental data specifically for anode fall and other energy loss mechanisms. Further extension into the azimuthal direction is also necessary in the future.

Acknowledgments

This work was supported by NASA GRC through a Ohio Aerospace Institute contract. The author was partially supported by Air Force Research Laboratory summer fellowship during the preparation of this paper.

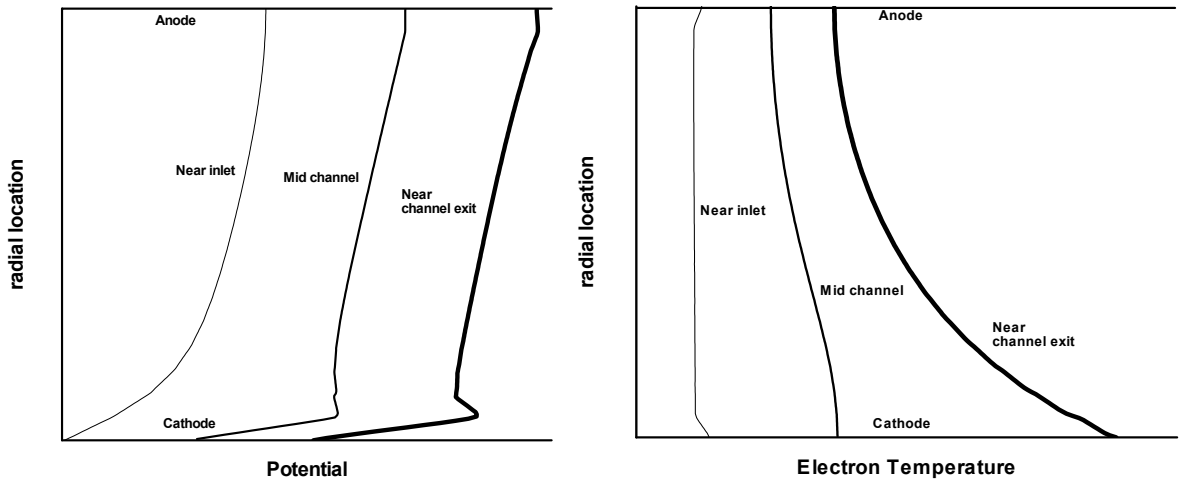

(a) Potential distribution (b) Electron temperature distribution

Figure 6. Potential and temperature distribution along the thruster cross-section at three axial locations.

References

[1]Peterkin, R.E., Jr., Frese, M.H., and Sovinec, C.R., Journal of Computational Physics, Vol. 140, pp. 148-171, 1998.

[2]R.E. Peterkin, Jr. and M.H. Frese, MACH: A Reference Manual – First Edition, Air Force Research Laboratory, Kirtland AFB, New Mexico, September 14, 1998.

[3]P.G. Mikellides, P.J. Truchi and N.F. Roderick, J. Propulsion and Power, **16** (5): 887-893 (2000).

[4]S. Roy, P.G. Mikellides and D.R Reddy, 40th AIAA Aerospace Science Meetings, AIAA-2002-0917, Reno, NV (Jan 2002).

[5]P.G. Mikellides, J. Propulsion and Power, **20** (2): 204-210 (2004).

[6]E. Choueiri, J. Propulsion and Power, **14** (5): 744-753 (1998).

[7]G. Caldo, Numerical simulation of MPD thruster flows with anomalous transport, Master's Thesis, Princeton University, 1994.

[8]K. Sankaran, E.Y. Choueiri and S.C. Jardin, J. Propulsion and Power, **20** (2004).

[9]M. Lapointe, Numerical simulation of self-field MPD thrusters, AIAA Paper No. 91-2341, 1991.

[10]P.C. Sleziona, M. Auweter-Kurtz and H.O. Schrade, Int. Journal for Numerical Methods in Engineering, **34**: 759–771 (1992).

[11]H. Kawaguchi, K. Sasaki, H. Itoh and T. Honma, Int. Journal of Applied Electromagnetics and Mechanics, **6**: 351–365 (1995).

[12]M. Auweter-Kurtz, C. Boie, H.J. Kaeppeler, et al., Int. J. of Applied Electromagnetics in Materials, **4**: 383–401 (1994).

[13]K.J. Berry and S. Roy, AIAA 39th Aerospace Sciences Meeting, AIAA-2001-0200, Jan. 2001.

[14]M. Tanaka and I. Kimura, Journal of Propulsion and Power, **4** (5): 428–436 (1988).

[15]S. Roy and B.P. Pandey, AIAA-02-2169, 33rd Plasma Dynamics and Lasers Conference, May 2002.

[16]S. Roy, B.P. Pandey, J. Poggie and D. Gaitonde, Physics of Plasmas, **10** (6): 2578-2585 (2003).

[17]L. Oksuz and N. Hershkowitz, Physical Review Letters **89**: 145001 (2002).

[18]V.A. Godyak and N. Sternberg, *IEEE Trans. on Plasma Science*, **18**(1): 159-168 (1990).

[19]S. Roy and B.P. Pandey, J. Propulsion and Power, 19 (5): 964-971 (2003).

[20]V.B. Tikhnov, S.A. Semenihin, V.A. Alexandrov, et al., IEPC-93-076, Electric Propulsion Society, Worthington, OH 1993.

[21]S. Roy and B.P. Pandey, Journal of Plasma Physics, **68** (4): 305-319 (2002).

[22]S. Roy and B.P. Pandey, Physics of Plasmas, **9** (9): 4052-4060 (2002).

[23]S. Roy, R. Raju, H. F. Chuang, B. Cruden and M. Meyyappan, *Journal of Applied Physics,* **93**, 4869 (2003).

[24]S. M. Cooper, B. A. Cruden, M. Meyyappan, R. Raju and S. Roy, *Nano Letters*, **4**, 377 (2004).

[25]S. Roy and B. Cruden, AIAA-2004-2673, 34th Fluid Dynamics and 37thThermophysics Conference, Portland, OR (2004).

[26]R. G. Jahn, W. F. von Jaskowsky, and K. E. Clark. Pulsed Electromagnetic Acceleration, *MAE Report*, 1467a, 1979.

[27]E.Y. Choueiri and J.K. Ziemer, *Journal of Propulsion and Power*, 17:967–976, 2001. September-October.